Energy Advances

ROYAL SOCIETY OF CHEMISTRY

PAPER

View Article Online
View Journal | View Issue

Cite this: *Energy Adv.*, 2025, 4, 447

Evaluating the potential of $Pr_2O_3/C_{18}H_6Cu_3O_{12}$ composites as positrodes with sustainable energy-power density for battery-supercapacitor hybrids

Muhammad Zahir Iqbal, *[a] Ayesha Zakir,[a] Syed Johar Ali Shah,[b] Ghulam Dastageer,[c] Khalid Mujasam Batoo[d] and Muhammad Farzik Ijaz[e]

Received 1st August 2024,
Accepted 16th January 2025

DOI: 10.1039/d4ya00490f

rsc.li/energy-advances

Hybrid supercapacitors (HSCs), incorporating the benefits of batteries and supercapacitors (SCs), have drawn significant research attention. In this regard, metal oxides and metal–organic frameworks (MOFs) have emerged as standout contenders for electrode materials because of their varying oxidation states, redox-active nature and immensely high porosity along with large active site ratios. Here, we fabricated praseodymium sesquioxide (Pr_2O_3) in combination with $C_{18}H_6Cu_3O_{12}$ MOF and compared their composites in different weight ratios. Through three-electrode characterizations, the composite with the same weight ratio revealed a remarkable specific capacity of 2046 C g^{-1}, showing enhanced performance because of the proper utilization of $C_{18}H_6Cu_3O_{12}$ porosity and the chemical activity of Pr_2O_3. This composite ($Pr_2O_3/C_{18}H_6Cu_3O_{12}$) was subsequently combined with activated carbon in a hybrid device, and numerous electrochemical characterizations were further performed. Based on the outcomes, the device demonstrated a maximum specific capacity of 310 C g^{-1}, along with energy and power densities of 67 W h kg^{-1} and 6114 W kg^{-1}, respectively, and a capacity retention of 98%. After careful evaluation of the device, two different models were applied to estimate the approximate capacitive and diffusive contributions of the device. These findings highlight the potential of the study for future usage in battery-supercapacitor systems.

1. Introduction

Rapid progress in industries, such as vehicles and telecommunications, has enormously increased energy demands.[1,2] The persistent reliance on natural resources has brought a drastic decline in their volume. Boundless consumption of fossil fuels has resulted in excessive CO_2 emission, which severely affect the ecosystem.[3] To overcome these energy crises caused by diminishing natural reserves, research efforts are focused on transitioning to sustainable and clean resources, such as solar and tidal energies.[4,5] However, these sources have inconsistent supply, which needs to be extenuated by establishing storage systems to perpetually harness this energy. Energy storage devices (ESDs) are the best alternatives to serve this purpose because of their efficiency, cost effectiveness and environmentally friendly behavior.[6,7] Based on storage mechanisms, ESDs are mainly classified into SCs and batteries. SCs store energy through physical adsorption by virtue of fast electrostatic charge transfer, whereas batteries work *via* reversible redox-driven chemical processes, which account for charge accumulation at the electrode–electrolyte interface.[8,9] Although SCs possess greater power, their inferior energy density hampers their performance. Batteries, on the other hand, prevail over SCs in energy storing ability but fall short in power density and cyclic stability.[10] To achieve better electrochemical performance, HSCs have been developed by assembling SCs and battery-grade electrodes into a single device.[11,12] In this regard, the fabrication of suitable electrode materials plays a decisive role in determining the performance of these hybrid devices.[13] In HSCs, carbonaceous materials with a large surface area are usually used as supercapacitive electrodes, while redox-active materials, such as conducting polymers and metal oxides, are utilized for battery-grade electrodes.[14–16] Conductive polymers exhibit better conductivity, but their mechanical instability halts their commercial exploitation as electrode materials.[17]

[a] *Renewable Energy Research Laboratory, Faculty of Engineering Sciences, Ghulam Ishaq Khan Institute of Engineering Sciences and Technology, Topi, 23640, Khyber Pakhtunkhwa, Pakistan. E-mail: zahir@giki.edu.pk*
[b] *Department of Physics Government Post Graduate College, Mansehra, 21300, Pakistan*
[c] *Department of Physics and Astronomy, Sejong University, Seoul 05006, South Korea*
[d] *King Abdullah Institute for Nanotechnology, King Saud University, P. O. Box-2455, Riyadh-11451, Saudi Arabia*
[e] *Department of Mechanical Engineering, College of Engineering, King Saud University, P. O. Box-800, Riyadh-12372, Saudi Arabia*

Owing to their natural abundance, high specific capacitance, enhanced stability, and wide operating potential range, metal oxides are extensively employed as redox-active electrodes in HSCs.[18,19]

Rare-earth metal-based materials are being explored for HSCs due to their unique 4f electronic configuration, varying oxidation states and stoichiometric deviations.[20,21] Studies suggest that the composition of transition metal oxides with rare-earth metal oxides strikingly enhanced their specific capacitances.[22–24] Some rare-earth metal oxides were used as electrodes and expressed fine electrochemical performance.[25,26] For instance, N. Maheswari *et al.*[27] prepared cerium oxide hexagonal nanostructures, which upon electrochemical characterizations yielded a remarkable specific capacitance of 523 F g^{-1} with 82% retention after 2000 cycles. Among metal oxides, praseodymium sesquioxide (Pr_2O_3) is thermally stable and shows Pr^{3+} and Pr^{4+} oxidation states.[28,29] It is the redox activity and high oxygen mobility facilitated by ultrafast switching between the two oxidation states that make it favorable for supercapacitor applications.[30] However, Pr_2O_3 suffers from exiguous conductivity and insufficient active site ratio, which circumscribe its electrochemical activity.[31] Its electrical conductivity lies in the range of 10^{-4} to 10^{-2}. To overcome this limitation, Pr_2O_3 can be assorted with MOFs.

MOFs are novel crystalline materials which constitute metal ions linked by organic ligands. Properties such as exceptional tunable porosity, high specific surface area and structural control boost their applications in HSCs.[32] Copper benzene tricarboxylate ($C_{18}H_6Cu_3O_{12}$) is a Cu-based MOF with trimesic acid (1,3,5-benzene tricarboxylic acid) as the linker. Nur Hawa *et al.*[33] hydrothermally synthesized $C_{18}H_6Cu_3O_{12}$ and assembled it in a device with nitrogen-doped graphene. The calculated energy and power densities were 2.61 W h kg^{-1} and 300 W kg^{-1}, respectively. The electrical conductivity of $C_{18}H_6Cu_3O_{12}$ is 10^{-8} to 10^{-4} S cm^{-1}. The excellent performance of $C_{18}H_6Cu_3O_{12}$ was attributed to its significantly high porosity and surface area. In the framework of $C_{18}H_6Cu_3O_{12}$, the Cu atom is attached to four oxygen atoms of the linker. The further existence of water molecules in its structure is responsible for providing a coordinative void on Cu species.

Herein, we report and compare pure Pr_2O_3, $C_{18}H_6Cu_3O_{12}$ and their composites in different weight ratios of 50/50, 75/25 and 25/75. These fabricated electrodes are then used as battery-type electrode materials for HSC applications. Before the electrochemical analysis, XRD, SEM and EDX were performed to probe the structural and crystalline properties of materials. After that, the electrochemical performance of these electrodes was investigated by CV, GCD and EIS in a three-electrode assembly. The best performing electrode was then used in a hybrid device with activated carbon as the counter electrode. The device delivered an enhanced electrochemical performance because of the synergistic effect produced by the high porosity of $C_{18}H_6Cu_3O_{12}$ and the redox activity of Pr_2O_3.

2. Experimental

2.1 Materials

Praseodymium sesquioxide (Pr_2O_3), $C_{18}H_6Cu_3O_{12}$, polyvinylidene fluoride (PVDF), carbon black and *N*-methyl-2-pyrrolidone (NMP) were bought from Sigma Aldrich. The materials were used as received without any further purification.

2.2 Synthesis of MOFs and electrode fabrication

For the synthesis of MOFs, the hydrothermal process was adapted. In short, 30 mL of DI water was used to disperse 7 mM cupric nitrate hemipentahydrate ($Cu_2H_{10}N_4O_{17}$). Following that, a solution of two equal parts (30 mL) of DI water and ethanol was combined to mix a trimesic linker of 3.5 mM. Prepared solutions were further poured into a 100 mL autoclave after vigorous stirring to ensure complete dissolution. The autoclave was then kept at 130 °C for twenty-four hours in an oven. Tiny crystals appeared once the autoclave was allowed to cool down to room temperature. Afterwards, the bluish crystals were separated from the mixture using a centrifuge. After continuously cleaned with ethanol, acetone, and DI water, the resulting material was dried in an oven. Further, for the fabrication of electrodes, nickel foam substrates were washed with ethanol, methanol, acetone, hydrochloric acid and deionized water. These substrates were then kept in a furnace to dry for 4 h. The active materials were taken with five different $Pr_2O_3/C_{18}H_6Cu_3O_{12}$ ratios, *i.e.* 100/0 (pristine Pr_2O_3), 50/50, 75/25, 25/75, and 0/100 (pristine $C_{18}H_6Cu_3O_{12}$), which were named as Pr_2O_3 and $C_{18}H_6Cu_3O_{12}$, $Pr_2O_3/C_{18}H_6Cu_3O_{12}$ (50/50), $Pr_2O_3/C_{18}H_6Cu_3O_{12}$ (25/75) and $Pr_2O_3/C_{18}H_6Cu_3O_{12}$ (75/25), respectively. These materials were mixed with carbon black and a PVDF binder in the ratio of 8/1/1. The slurries were prepared by dissolving these mixtures into NMP and stirring the solution for 8 h. Five working electrodes were fabricated by depositing these slurries onto Ni foam substrates followed by drying in an oven for 4 h at 90 °C. The flowchart illustration of the synthesis of MOF and fabrication of electrode is depicted in Fig. 1.

2.3 Characterizations

X-ray diffraction was performed to investigate the crystallinity and phase purity of the samples. To study the morphology and structure, SEM images were acquired. Cyclic voltammetry (CV), galvanostatic charge–discharge (GCD), and electrochemical impedance spectroscopy (EIS) were carried out to examine the electrochemical performance of all the samples in the three-electrode assembly. The three-electrode setup was designed using the working electrodes with functioning Mercury/mercury-oxide (Hg/HgO) and platinum wire (Pt-wire) as the reference and counter electrodes in 1 M potassium hydroxide (KOH) electrolyte. The real device was then manufactured by integrating the best performing electrode with activated carbon as the counter electrode. CV, GCD and EIS measurements were performed for this device.

3. Results and discussion

3.1 Structural characterizations

Employing a prototype X-ray diffraction framework, the structural characteristics of the material were identified. The arrangement used a radiation source of Cu-Kα at room temperature, at an accelerating voltage, tube current, and step size of 40 kV, 25 mA, and 0.05°, to obtain the structural data related to material

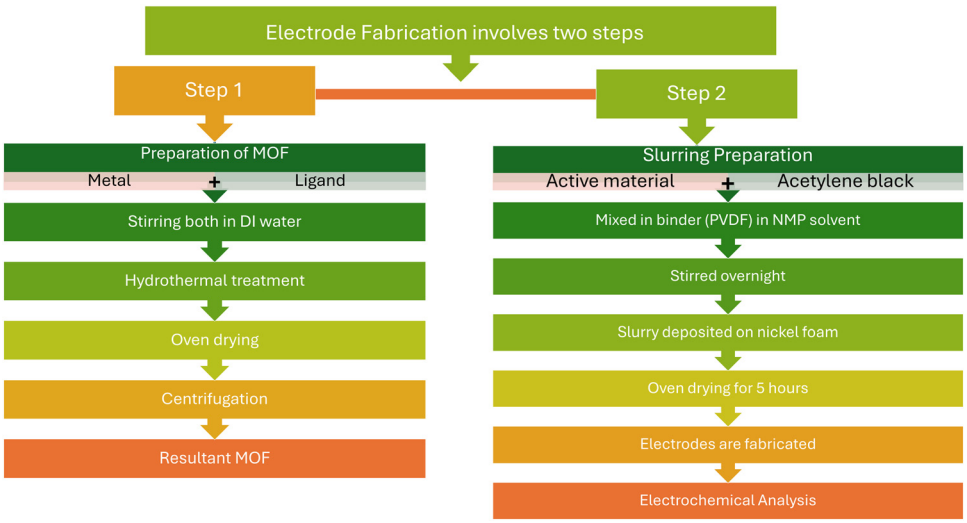

Fig. 1 Synthesis of MOFs and the fabrication process of electrodes.

deposition. The data were obtained *via* scanning ranges from 20° to 80°. The XRD data were collected three times to ensure uniformity. Fig. 2(a) illustrates the diffractograms of Pr_2O_3 and $C_{18}H_6Cu_3O_{12}$. The XRD analysis unveiled distinguishing peaks for Pr_2O_3 at 2θ values of 28°, 30°, 40°, and 49°, corresponding to the (002), (101), (110), and (210) planes respectively. These peaks perfectly reflect the reference (JCPDS: #42-1121).[34] The XRD analysis of the $C_{18}H_6Cu_3O_{12}$ displays a significant peaks centered at an angle of 21.13°, 22.32°, 23.2°, 25.8°, 27.3°, 28.5°, 37.3°, and 46.82°, correlating the (440), (620), (640), (444), (551), (773), and (882) planes respectively. These peaks matched the reference (PDF#00-062-1183) database.

3.2 Morphological analysis

SEM was used for examining the surface morphology of the fabricated electrodes. The micrograph of Pr_2O_3, and $C_{18}H_6Cu_3O_{12}$ can be seen in Fig. 2(b) and (c). For $C_{18}H_6Cu_3O_{12}$, the micrographs showed a flake-like morphology, a crucial characteristic for supercapacitor applications. By enhancing the required transportation of ions in the electrode's matrix, this flaky configuration promotes fast charge and discharge kinetics, boosting the material's capabilities of storing charge and ionic conductivity. Furthermore, the crystalline structure of Pr_2O_3 may aid in the efficient transfer of carriers and charge, minimizing the internal resistance and boosting the energy storage capacity. Moreover, it can minimize the morphological deterioration by supporting ion dissemination as well as adsorption. Both factors can improve the long-term durability of the supercapacitor. The composite then showed the presence of Pr_2O_3 and $C_{18}H_6Cu_3O_{12}$, integrating their crystalline and flaky features, which result in increased surface area and active sites. These results are verified by further electrochemical findings.

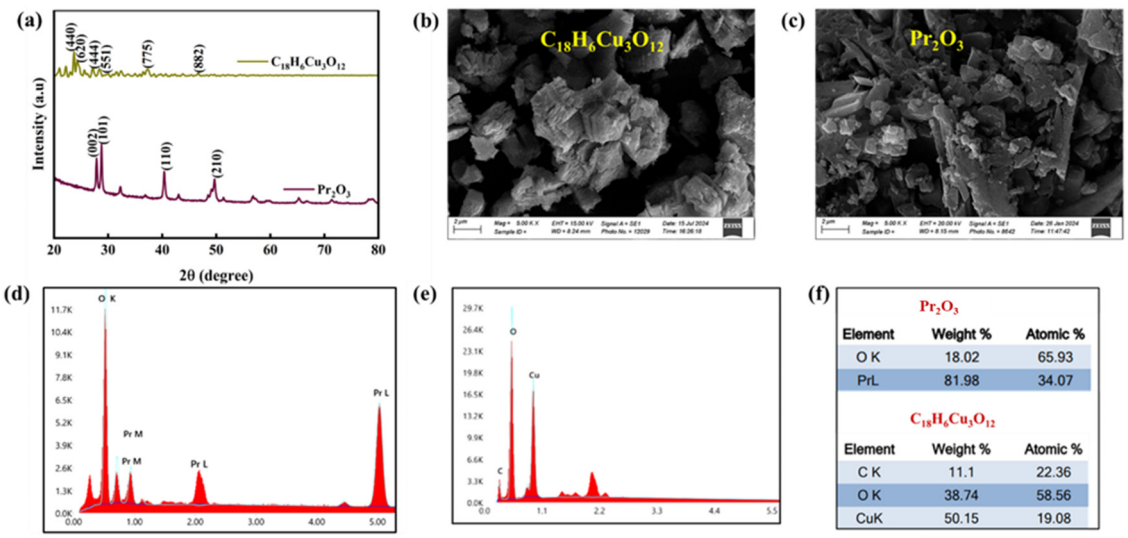

Fig. 2 (a) X-ray diffractograms of Pr_2O_3 and $C_{18}H_6Cu_3O_{12}$. Scanning electron microscopic micrographs of (b) $C_{18}H_6Cu_3O_{12}$ and (c) Pr_2O_3. Energy-dispersive X-ray spectra of (d) Pr_2O_3, and (e) $C_{18}H_6Cu_3O_{12}$. (f) Atomic and weight percentage contributions of Pr_2O_3 and $C_{18}H_6Cu_3O_{12}$.

3.3 Elemental analysis

After examining the physical characteristics of the fabricated electrodes, elemental analysis was performed using EDX. The EDX outcomes for Pr_2O_3 are shown in Fig. 2(d), confirming the presence of both oxygen and praseodymium. Following that, Fig. 2(e) depicts the chemical composition of $C_{18}H_6Cu_3O_{12}$, which is composed of carbon, copper, and oxygen.

Afterwards, the atomic and weight percentages of elements in Pr_2O_3 and $C_{18}H_6Cu_3O_{12}$ are depicted in Fig. 2(f). The oxide was acquired from an accredited supplier (Sigma Aldrich), and its elemental composition was determined by EDX on the as-received granules. EDX gives semi-quantitative data rather than precise quantification owing to a variety of circumstances. The approach analyses by matching the observed X-ray intensities of the sample to those of reference standards; consequently, the findings are reliant on calibration, sample set up, and experimental parameters.

Because EDX predominantly studies a sample's surface or near-surface area, with an interaction that goes down to a few micrometres, it may not accurately represent the bulk arrangement. The detected variation in the stoichiometric percentage of Pr_2O_3 can be attributed to changes in the probability cross-section for the emission of X-rays among praseodymium (Pr) and oxygen (O). Additionally, matrix impacts, which occur when the composition of one element impacts the exhalation and recognition of X-rays from a different one, can have an impact on accuracy. To eliminate the undiscovered items, which can potentially lead to data skewing, EDX normally normalizes the findings to 100% for identified elements.

The findings of EDX in our study indicate that the composition approximately matches that of stoichiometric Pr_2O_3, which was earlier identified by the XRD.

4. Electrochemical analysis

4.1 Three-electrode assembly

4.1.1 Cyclic voltammetry. By delivering a potential pulse to the electrode during CV monitoring, one may determine if redox processes are reversible or irreversible. This strategy aids in the evaluation of electrode materials *via* offering details on the electrode dimensions, deposited species, and the rate of reaction, and this strategy aids in the evaluation of electrode materials. The electrochemical characteristics of the positive electrodes in a three-cell configuration were investigated using a counter-electrode of platinum wire and a reference of Hg/HgO. Initially, the material was tested and activated using fifteen CV cycles at 3 mV s^{-1}. Further, the CV of the electrodes was conducted at different scan rates at a constant potential window of 0–0.7 V using a Gamry reference 3000 potentiostat. The units of each parameter are illustrated in Table 1.

The CV curves of Pr_2O_3 and $C_{18}H_6Cu_3O_{12}$, $Pr_2O_3/C_{18}H_6Cu_3O_{12}$ (50/50), $Pr_2O_3/C_{18}H_6Cu_3O_{12}$ (25/75) and $Pr_2O_3/C_{18}H_6Cu_3O_{12}$ (75/25) are represented in Fig. 3(a)–(e). The obtained voltammograms expressed clear redox peaks depicting the battery-grade nature of the electrode material. These peaks infer the occurrence of redox reactions between the electrode's active material and the OH^- ions of electrolytes.[35] The curve shapes at the lowest and highest scan rates were analyzed to predict the rate capability. For these samples, a notable shift in peaks was observed with an increment in scan rates. Furthermore, the shape of all the samples persists as unaffected at low scan rates, indicating the electrodes' phenomenal resilience, with the sole exception of a variance in select peak positions. However, there is a minimal change noted at high scan rates owing to the incompetence of ions to complete the reaction. These voltammogram patterns show that the mass transport rate was the governing factor in diffusion-regulated processes. This highlights the potential value of electrodes in electrochemical processes by proving their capacity to perform rapid and reversible faradaic reactions. However, from Fig. 3(f), it is clear that the material with an equal ratio appears to sustain its shape with least distortion at elevated scan rates, indicating relatively better rate capability. Pr_2O_3 and $C_{18}H_6Cu_3O_{12}$ have a minimum area under the curve, which demonstrates its meagre capacity, while areas enclosed by the composites are much greater, and thus, they have attained high capacities.

Table 1 Units of each parameter used in the measurements

S. no	Name	Units
1	Scan rate	mV s^{-1}
2	Current density	A g^{-1}
3	Specific capacity	C g^{-1}
4	Energy density	W h kg^{-1}
5	Power density	W kg^{-1}

The further examination of the CV curves gives substantial insights into the electrochemical behaviour, specifically the polarization effects and shifts in the reduction peaks. The increased polarization at higher scan rates indicates a higher charge transfer resistance, which can occur when the kinetics of redox reactions cannot keep pace with the faster potential sweep rates. The polarization of the peak in the CV curve for the composites of Pr_2O_3 and $C_{18}H_6Cu_3O_{12}$ indicates that multiple electrochemical processes are occurring simultaneously, reflecting a more complex redox behavior than observed in the individual components.

The CV curve of the oxide shows an oxidation peak at 0.55 V and a pair of reduction peaks at 0.42 V and 0.49 V, suggesting limited redox activity due to the low surface area, as reflected in the relatively low current response of 18 mA. Conversely, the MOF demonstrates a higher oxidation peak of 0.60 V and reduction peaks at 0.48 V and 0.32 V, with a significant current of up to 61 mA, indicating enhanced electrochemical activity. However, the sharp rise in current after the peak may indicate increased polarization, especially at higher scan rates.

The presence of both materials introduces different redox couples within the composite; Pr_2O_3 can participate in oxidation and reduction reactions involving changes in the oxidation states of Pr (from +3 to +4), while $C_{18}H_6Cu_3O_{12}$ may engage in ligand-based electron transfer or redox processes involving its metal centers. This enhances the overall surface area and increases the density of active sites available for electrochemical reactions, leading to a more distributed reaction environment

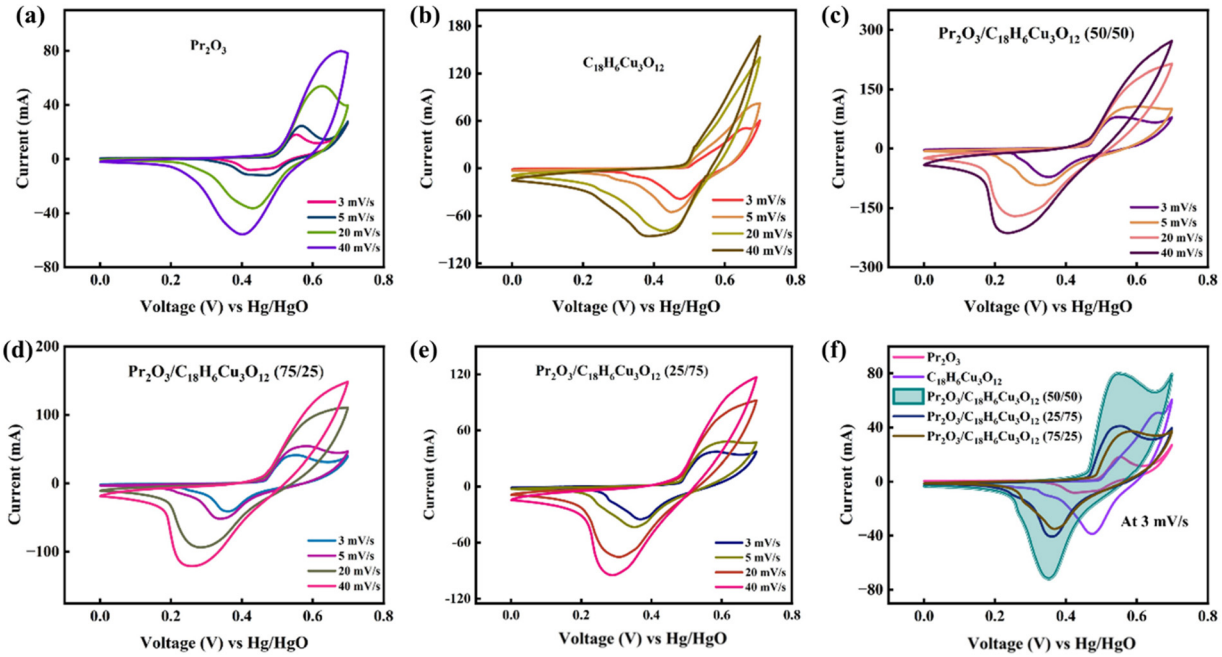

Fig. 3 Cyclic voltammograms of (a) Pr_2O_3, (b) $C_{18}H_6Cu_3O_{12}$, (c) $Pr_2O_3/C_{18}H_6Cu_3O_{12}$ (50/50), (d) $Pr_2O_3/C_{18}H_6Cu_3O_{12}$ (75/25), and (e) $Pr_2O_3/C_{18}H_6Cu_3O_{12}$ (25/75). (f) Comparison of all the samples' voltammograms at 3 mV s^{-1}.

that contributes to polarization. Additionally, the blending may facilitate improved electron transfer and ion mobility, resulting in a more heterogeneous charge distribution throughout the composite. This can create variations in the local electrochemical activity, where different regions of the composite exhibit distinct kinetic properties, leading to a less sharp peak in the CV curves. Overall, the observed broadening signifies that the composite effectively combines the unique properties of both materials, enhancing the overall electrochemical performance. The CV curve of the oxide shows an oxidation peak at 0.55 V and a pair of reduction peaks at 0.42 V and 0.49 V, suggesting limited redox activity due to the low surface area, as reflected in the relatively low current response of 18 mA. Conversely, the MOF demonstrates a higher oxidation peak of 0.60 V and reduction peaks at 0.48 V and 0.32 V, with a significant current of up to 61 mA, indicating enhanced electrochemical activity.

The $Pr_2O_3/C_{18}H_6Cu_3O_{12}$ (50/50) blend shows an oxidation peak at 0.52 V and a reduction peak at 0.36 V, with a current of 69 mA, suggesting improved electron transfer due to the synergistic effects of blending. Further, in $Pr_2O_3/C_{18}H_6Cu_3O_{12}$ (75/25), the oxidation peak at 0.53 V and the reduction peak at 0.35 V indicate some improvement over the oxide alone, while the emergence of a new peak suggests the formation of a new redox couple due to the interaction between the two materials. Finally, the $Pr_2O_3/C_{18}H_6Cu_3O_{12}$ (25/75) configuration displays an oxidation peak of 0.56 V and a reduction peak of 0.36 V, along with a new redox peak at 0.27 V, indicating additional redox processes. The blended materials exhibit a similar behaviour to Pr_2O_3 in the positive scan and $C_{18}H_6Cu_3O_{12}$ in the negative scan, with a peak shifting at high scan rates due to their synergistic impact.

4.1.2 Galvanostatic charge–discharge. After analysing the electrode charge storing process *via* CV, we further implied GCD analysis to obtain information about the charge and discharge process of the electrodes. It is an essential technique for evaluating the electrochemical characteristics of different materials such as energy and power density as well as specific capacity, for the purpose of evaluating the effectiveness of the device. GCD makes it simpler to study the mechanisms of shifting charges and the dissemination of ions in various electrode materials since it continuously supplies and records current as well as voltage fluctuations to the electrodes. GCD plots of Pr_2O_3 and $C_{18}H_6Cu_3O_{12}$, $Pr_2O_3/C_{18}H_6Cu_3O_{12}$ (50/50), $Pr_2O_3/C_{18}H_6Cu_3O_{12}$ (25/75) and $Pr_2O_3/C_{18}H_6Cu_3O_{12}$ (75/25) are illustrated in Fig. 4(a)–(e). These trends showed an increasing spike and dip in voltage throughout charging and discharging, respectively. This indicates that the materials have a relatively stable voltage profile. Additionally, all the samples' GCD curves showed noticeable plateaus in the charge–discharge curves, indicating the existence of faradaic processes between the active material and electrolyte ions. The well-defined plateaus in the GCD curves of the blended materials, compared to the less evident plateaus in Pr_2O_3 and $C_{18}H_6Cu_3O_{12}$ separately, indicated the emergence of a more battery-dominant charge storage mechanism in the composite. The combination of Pr_2O_3 with $C_{18}H_6Cu_3O_{12}$ may modify electron and ion transport mechanisms, resulting in electrochemical channels where faradaic redox processes dominate charge storage. The redox processes in $C_{18}H_6Cu_3O_{12}$ metal centres or ligands and different oxidation states of Pr (Pr^{3+}/Pr^{4+}) resulted in separate plateaus in the GCD curves, showing persistent and improved redox activity.

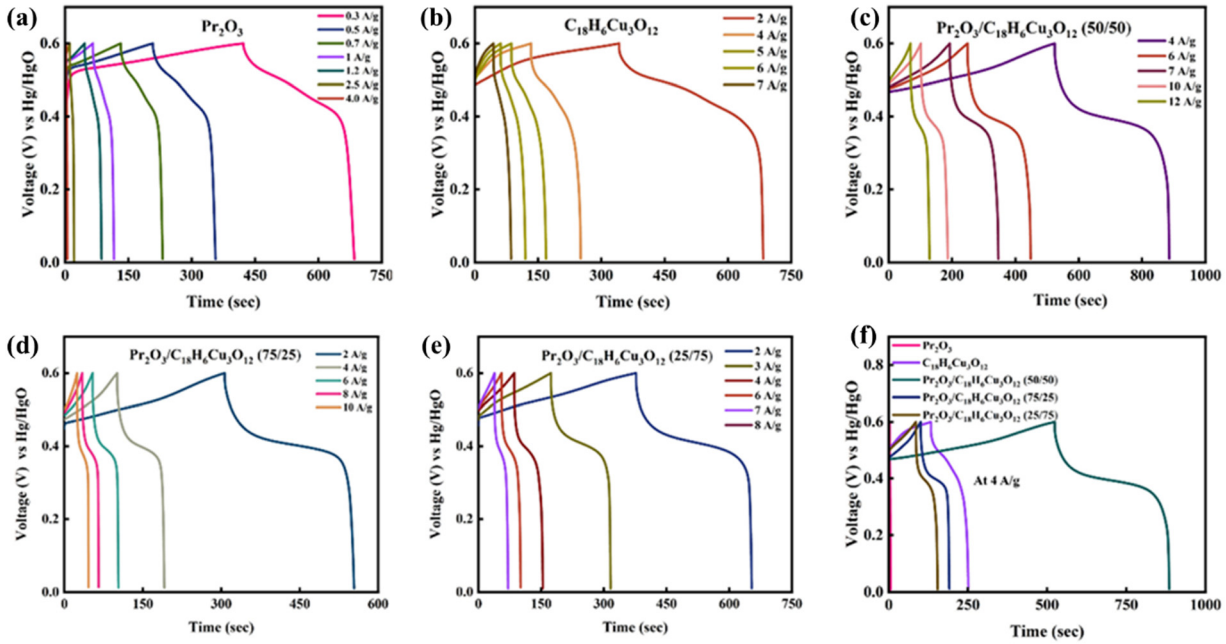

Fig. 4 Galvanostatic charge–discharge curves of (a) Pr_2O_3, (b) $C_{18}H_6Cu_3O_{12}$, (c) $Pr_2O_3/C_{18}H_6Cu_3O_{12}$ (50/50), (d) $Pr_2O_3/C_{18}H_6Cu_3O_{12}$ (75/25), (e) $Pr_2O_3/C_{18}H_6Cu_3O_{12}$ (25/75). (f) Comparison of all the samples' GCD curves at 4 A g^{-1}.

The IR drop of pristine MOFs and oxides is 0.049 V and 0.055 V, whereas for $Pr_2O_3/C_{18}H_6Cu_3O_{12}$ (50/50), $Pr_2O_3/C_{18}H_6Cu_3O_{12}$ (25/75) and $Pr_2O_3/C_{18}H_6Cu_3O_{12}$ (75/25), it is 0.16 V, 0.18 V and 0.15 V, respectively, which might be brought about by slower ion kinetics or modifications in the composite's conductivity. This would represent more battery-like behaviour, where ions are inserted and removed from active sites more slowly. The blend's possible interparticle interactions and capacitive and faradaic characteristics combine to further increase the electrochemical activity and produce clearer plateaus.

Further, the activation and ohmic polarization during discharge have a substantial impact on the electrochemical performance of battery-type electrodes. Activation polarization occurs as a result of the energy required to start electrochemical processes at the electrode–electrolyte interface, which reduces energy efficiency. Ohmic polarization occurs owing to internal resistance, resulting in a voltage decrease upon discharge. Larger droplets imply increased internal resistance and slower ion/electron movement. Understanding and limiting these polarizations are critical for optimizing energy storage device performance.

The ohmic drop varies greatly among samples, providing valuable insights into their internal resistances and electrochemical performance. The oxide electrode has the greatest ohmic drop from 0.55 V to 0.39 V (440 s to 650 s), showing significant internal resistance that reduces performance. The MOF electrode has a comparable range, with an ohmic drop of 0.54 V to 0.37 V (347 s to 658 s), but its longer discharge time indicates significantly better conductivity than the oxide.

Among the composite samples, the 50/50 MOF-oxide mix exhibits a more gradual and protracted ohmic drop from 0.44 V to 0.35 V (556 s to 827 s), indicating the lowest internal resistance and the highest electron/ion transport, greatly improving performance. The 75% oxide/25% MOF blend exhibits a quick ohmic decrease from 0.44 V to 0.35 V (350 s to 531 s), showing high resistance comparable to pure oxide, which reduces performance. Meanwhile, the 75% MOF/25% oxide mix experiences a reduction from 0.45 V to 0.34 V (429 s to 636 s), with a higher conductivity than the 75% oxide blend but less efficiency than the 50/50 blend. Overall, the synergistic effects between Pr_2O_3 and $C_{18}H_6Cu_3O_{12}$ drive the hidden chemistry behind these results, resulting in the formation of novel redox pathways, enhanced charge storage mechanisms, and a more complicated electrochemical performance than the separate materials.

With the elevated current density, the discharge period decreased due to the limited ion transfer between the electrode and the electrolyte interface, leading to a decline in efficiency.[36] The GCD plots are backing the CV results by showing the highest discharge time for $Pr_2O_3/C_{18}H_6Cu_3O_{12}$ (50/50) as shown from the comparison in Fig. 4(f).

4.1.3 Electrochemical impedance spectroscopy. After the analysis of the charge storing process and the charging–discharging behavior of electrodes, EIS spectra were recorded in the frequency range of 0.1–100 kHz to delve deep into the analysis of ion transfer kinetics and the determination of different resistances. The Nyquist plots of all the samples are represented in Fig. 5(a) with an inset zoomed image. The material experienced low equivalent series resistance (ESR) as evident from *x*-intercepts of the Nyquist plot.[37] The measured values of ESR from the *x*-intercept for Pr_2O_3 and $C_{18}H_6Cu_3O_{12}$, $Pr_2O_3/C_{18}H_6Cu_3O_{12}$ (50/50), $Pr_2O_3/C_{18}H_6Cu_3O_{12}$ (25/75) and $Pr_2O_3/C_{18}H_6Cu_3O_{12}$ (75/25) are 1.9 Ω, 1.6 Ω, 0.5 Ω, 1.5 Ω, and 0.75 Ω respectively. The smallest ESR value was achieved for

$Pr_2O_3/C_{18}H_6Cu_3O_{12}$ (50/50). The non-existence of a semi-circle in Nyquist plots implies the absence of charge transfer resistance, thus unveiling the substantial redox activity of materials.[38] The linear region at low frequencies discloses the capacitive nature of the electrode.

4.1.4 Electrochemical parameters. The electrochemical parameters from the CV and GCD were computed to obtain information on the specific capacity profiles of all the electrodes. Eqn (1) was used to find out the specific capacity of all electrodes from the CV:

$$Q_s = \frac{1}{mv}\int I\,dV \quad (1)$$

where m is the mass loading, v is the scanning rate, I is the peak current and integral is the area under the CV curve. The trend of specific capacity values *via* CV is depicted in Fig. 5(b). At 3 mV s^{-1} scan rate, maximum specific capacity values for pristine Pr_2O_3 and $C_{18}H_6Cu_3O_{12}$, $Pr_2O_3/C_{18}H_6Cu_3O_{12}$ (25/75) and $Pr_2O_3/C_{18}H_6Cu_3O_{12}$ (75/25) were calculated to be 238 C g^{-1}, 799 C g^{-1}, 929 C g^{-1} and 1032 C g^{-1}, respectively. The sample with an equal concentration of Pr_2O_3 and $C_{18}H_6Cu_3O_{12}$ yields the highest specific capacity of 2046 C g^{-1}. The comparison of this work with those previously reported in the literature is presented in Table 2. These findings can be justified by the claim that $C_{18}H_6Cu_3O_{12}$ provided a huge ratio of active sites, which were used by redox active Pr ions for faradaic reactions, thus resulting in a surreal specific capacity. While in other weight ratios, the individual nature dominates and therefore appropriate synergy is not achieved. The decreasing trend of capacities with increasing scan rates testifies their inverse relations. Furthermore, the specific capacities were calculated using the GCD data at different current densities and their corresponding discharge times using eqn (2):

$$Q_s = \frac{1}{m}(I \times t) \quad (2)$$

where I, Δt and m represent the current, discharge time, and mass respectively. Similar to CV calculations, $Pr_2O_3/C_{18}H_6Cu_3O_{12}$ (50/50) revealed the highest specific capacity of 1539 C g^{-1} at a current density of 3 A g^{-1}, whereas the maximum measured capacities for Pr_2O_3, $Pr_2O_3/C_{18}H_6Cu_3O_{12}$ (75/25), $Pr_2O_3/C_{18}H_6Cu_3O_{12}$ (25/75) and $C_{18}H_6Cu_3O_{12}$ were 90 C g^{-1}, 602 C g^{-1}, 450 C g^{-1}, and 524 C g^{-1}, respectively. The drop in specific capacities at high current densities is because of the insufficient time for charges to undergo faradaic reactions.[39] Fig. 5(c) displays specific capacity vs current density plots for all samples. The decline in the capacity of $Pr_2O_3/C_{18}H_6Cu_3O_{12}$ (50/50) is not abrupt; rather, it varies gradually with the current density, signifying its high-rate capability.

From these characterizations, $Pr_2O_3/C_{18}H_6Cu_3O_{12}$ (50/50) has the highest capacity and rate capability with negligible resistance. Thus, it emerges to be a potential candidate for use as the battery-grade electrode in hybrid devices.

Table 2 Comparison of the capacities from this work with previously reported literature, using the electrolyte employed in the half-cell assembly

Material	Electrolyte	Specific capacitance/ capacity	Ref.
HKUST-1@$LaNiO_3$	KOH	786 F g^{-1}	40
CuO@Zn-Co-MOF	KOH	684 F g^{-1}	41
CuO@Ni-MOF	N/A	1455.75 F g^{-1}	42
Co_3O_4@Ni-MOF	KOH	1980.7 F g^{-1}	43
$NiCo_2O_4$@MOF-5	KOH	557.5 F g^{-1}	44
$NiCo_2O_4$@Ni-MOF	KOH	208.8 mA h g^{-1}	45
NiO@Ni-MOF	KOH	1853 C cm^{-2}	46
NiO@Ni-MOF-25	KOH	1176.6 F g^{-1}	47
CeO_2@ZIF-8	KOH	424.2 F g^{-1}	48
MnO_2@MnHCF	Na_2SO_4	225.6 F g^{-1}	49
NiO_2@CuHCF	Na_2SO_4	908 F g^{-1}	50
MnO_2@CoHCF	Na_2SO_4	385 F g^{-1}	51
MnO_2@NiHCF	Na_2SO_4	224 F g^{-1}	52
$Pr_2O_3/C_{18}H_6Cu_3O_{12}$ (50/50)	**KOH**	**2046 C g^{-1}**	**This work**

5. Electrochemical analysis of the hybrid device

After the evaluation of fabricated electrodes in half-cell configurations, the hybrid device was assembled by using $Pr_2O_3/C_{18}H_6Cu_3O_{12}$ (50/50) as the battery-grade (positive) electrode and activated carbon (AC) as the capacitive counter electrode in 1 M KOH solution. The visual graphic of the hybrid device is depicted in Fig. 6(a). The mass loading on both electrodes is done by using the following relation:

$$\frac{m_+}{m_-} = \frac{Cs_- \times \Delta V_-}{Cs_+ \times \Delta V_+} \quad (3)$$

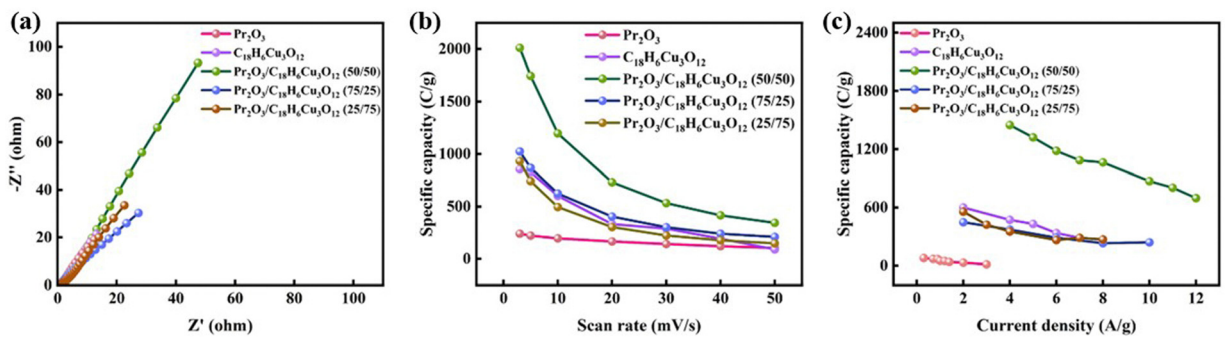

Fig. 5 (a) Electrochemical impedance spectroscopy of all samples. Trend of specific capacities through (b) CV and (c) GCD.

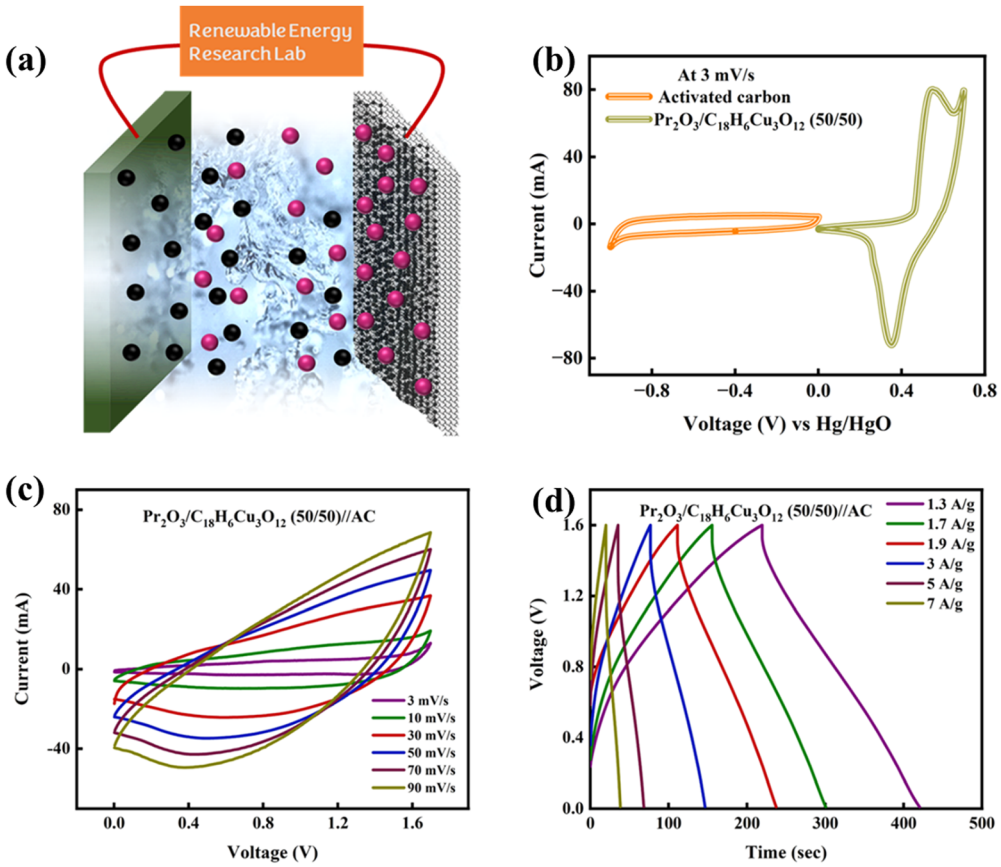

Fig. 6 (a) Schematic of the real device. (b) Comparison of CV curves of activated carbon and $Pr_2O_3/C_{18}H_6Cu_3O_{12}$ (50/50). (c) Cyclic voltammograms of $Pr_2O_3/C_{18}H_6Cu_3O_{12}$ (50/50)//AC. (d) Galvanostatic charge–discharge curves of $Pr_2O_3/C_{18}H_6Cu_3O_{12}$ (50/50)//AC.

In the above equation, m represents the mass loading for the positive and the negative electrode. Cs represents the specific capacitance, while ΔV represents the potential window for both electrodes. The positive and negative signs represent the intended parameters of the positive and negative electrodes.

The CV curve of AC in −1.0 to 0 V potential window expressed a rectangular shape, indicating the super-capacitive behavior, while the CV curve of the active material in the 0–0.7 V potential window demonstrates anodic and cathodic peaks, asserting its battery-grade nature, as represented in Fig. 6(b). CV was further carried out for the hybrid device at a combined potential window of 0–1.7 V at different scan rates. Fig. 6(c) presents the CV profiles of device at various scan rates from 3 mV s^{-1} to 50 mV s^{-1}. The CV curve revealed both rectangular shape and redox peaks, affirming the hybrid nature of device. The retention of shape at higher scan rates signifies the fine rate capability of the hybrid device. Afterwards, the GCD measurements were taken in 1–1.6 V potential window at multiple current densities. The GCD plots of device are demonstrated in Fig. 6(d). These profiles are compatible with earlier reported CV profiles as the presence of both linear and non-linear regions certifies the hybrid nature of this device. The fall in discharge time with up-rising current densities is an indicator of only the outer surface's contribution to charge storage because of inadequate time. The trend of specific capacity values of device at different current densities is depicted in Fig. 7(a). From the trend, it is clear that the highest specific capacity attained by the device is 310 C g^{-1} at a current density of 1.3 A g^{-1}. Afterwards, the EIS was proceeded on the device for in-depth inquisition of reaction kinetics and impedance evaluation. The Nyquist plot of the device along with its fitted model is depicted in Fig. 7(b). No semi-circle was observed in the plot, which uncovers the refined chemical activity of material. Further the capacity retention of the device is analyzed which shows that the device maintained 98% of its original value after 3000 GCD cycles as depicted in Fig. 7(c). The energy and power densities were further figured out using the following relations:

$$E = \frac{Q_s \times \Delta V}{7.2} \quad (4)$$

$$P = \frac{E}{\Delta t} \times 3600 \quad (5)$$

where E and P are the energy and power densities respectively. Q_s, Δt and ΔV are the specific capacity, discharge time and potential respectively. The device possessed the highest energy density of 67 W h kg^{-1} with a corresponding power density of 6114 W kg^{-1}, as shown in Fig. 7(d). The comparison of the

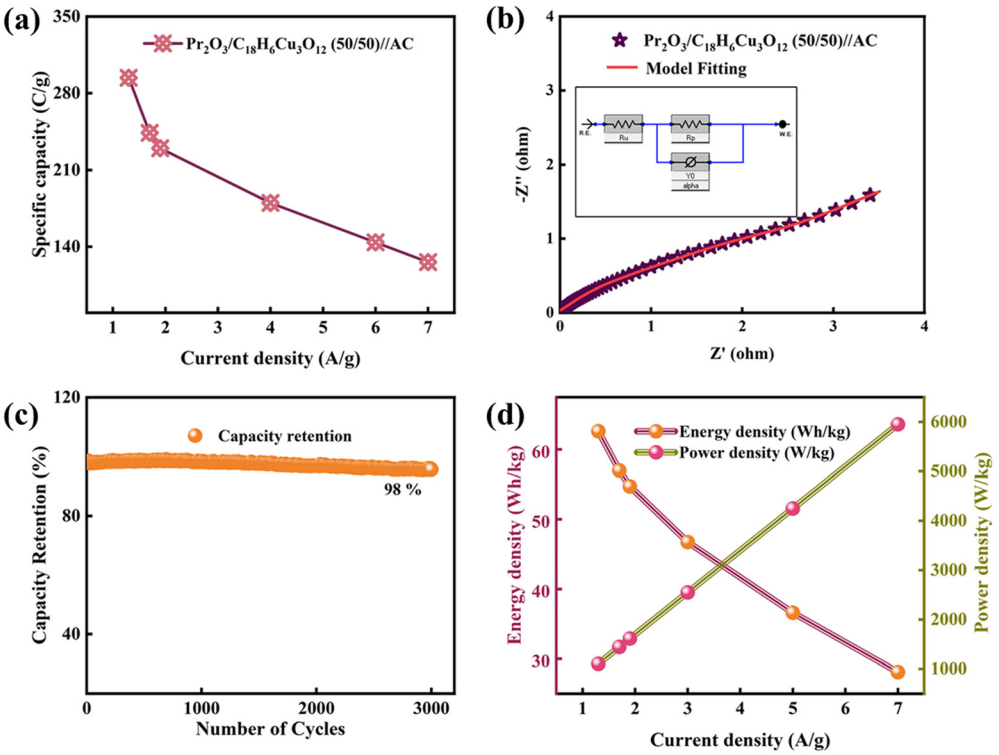

Fig. 7 (a) Specific capacity trend of the real device through GCD. (b) Nyquist plot of the device along with the fitted model. (c) Capacity retention of the device after 3000 GCD cycles. (d) Energy and power density of the device.

device performance with that previously reported in the literature is depicted in Table 3.

6. Quantifying capacitive and diffusive contributions of the device

After evaluating the device's electrochemical properties, we employed, examined, and then contrasted two distinct models, identified as the linear and quadratic models, to identify the best approximate values of the device's capacitive and diffusive contributions. The study clearly demonstrated the applicability of the quadratic model as it fitted on the experimental data.

Because of the combination of faradaic and non-faradaic responses, the device delivers two distinct currents from its two combined properties of batteries and capacitors. Non-faradaic events were caused by the presence of capacitive electrodes, which do not entail charge transfer behavior and instead rely on the double-layer effect, while the battery-graded electrode was accountable for the faradaic reactions that occur due to the material's ability to endure oxidation and reduction processes. Consequently, in the HSC, capacitive and diffusive effects evolve. Hence:

$$i(\nu, V) = i_{NF} + i_F = k_1(V)\nu + k_2(V)\nu^{\frac{1}{2}} \quad (6)$$

where ν is the scan rate, i is the total current and $i_{NF} + i_F$ shows the non-faradaic and faradaic reactions (diffusive). $k_1(V)\nu$ portrays the capacitive inclusions and the processes controlled by diffusion are designated by $k_2(V)\nu^{\frac{1}{2}}$. Further, the linear model is fitted on the actual experimental data of the device *via* adding the capacitive and diffusive contributions of the device, as depicted in Fig. 8(a)–(c), regardless of an effective attempt to imitate the experimental results. The model lacks to fit on many sections of the experimental values, particularly around

Table 3 Comparison of the capacitance, energy density and power density from this work with previously reported literature in full-cell assembly

Materials	Specific capacitance/capacity	Energy density	Power density	Ref.
CeO_2@ZIF-8	89 F g^{-1}	31.3 W h kg^{-1}	800 W kg^{-1}	48
$NiCo_2O_4$@Ni-MOF	41.5 mA h g^{-1} (149.6 C g^{-1})	32.6 W h kg^{-1}	348.9 W kg^{-1}	45
MnO_2@CoHCF	76.3 F g^{-1}	47.3 W h kg^{-1}	1100 W kg^{-1}	51
Ni-Co-ZIF/CuO	210 C g^{-1}	43 W h kg^{-1}	10 600 W kg^{-1}	53
Co/Cu-MOF&Cu_3O	82.14 F g^{-1}	25.67 W h kg^{-1}	3786.46 W kg^{-1}	54
TiO_2/Co-MOF	36 C g^{-1}	7.5 W h kg^{-1}	375 W kg^{-1}	55
NiO@Ni-MOF	144 F g^{-1}	39.2 W h kg^{-1}	7000 W kg^{-1}	46
$Pr_2O_3/C_{18}H_6Cu_3O_{12}$ (50/50)	**310 C g^{-1}**	**67 W h kg^{-1}**	**6114 W kg^{-1}**	**This work**

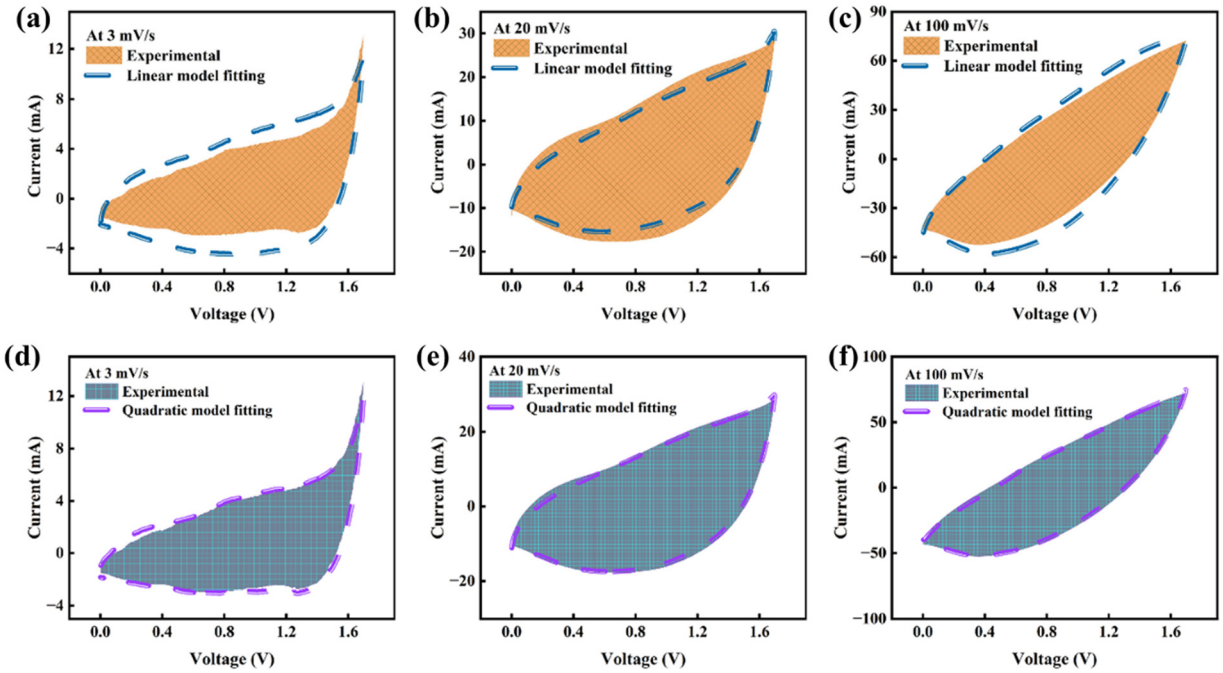

Fig. 8 (a)–(c) Linear model fitting on experimental data. (d)–(f) Quadratic model fitting on experimental data.

peaks and other sections, which contradicts the fundamental assumption of linearity. Applying a linear model under these conditions appears to go against the norm of what is acceptable. Therefore, to overcome the restrictions, we have added a

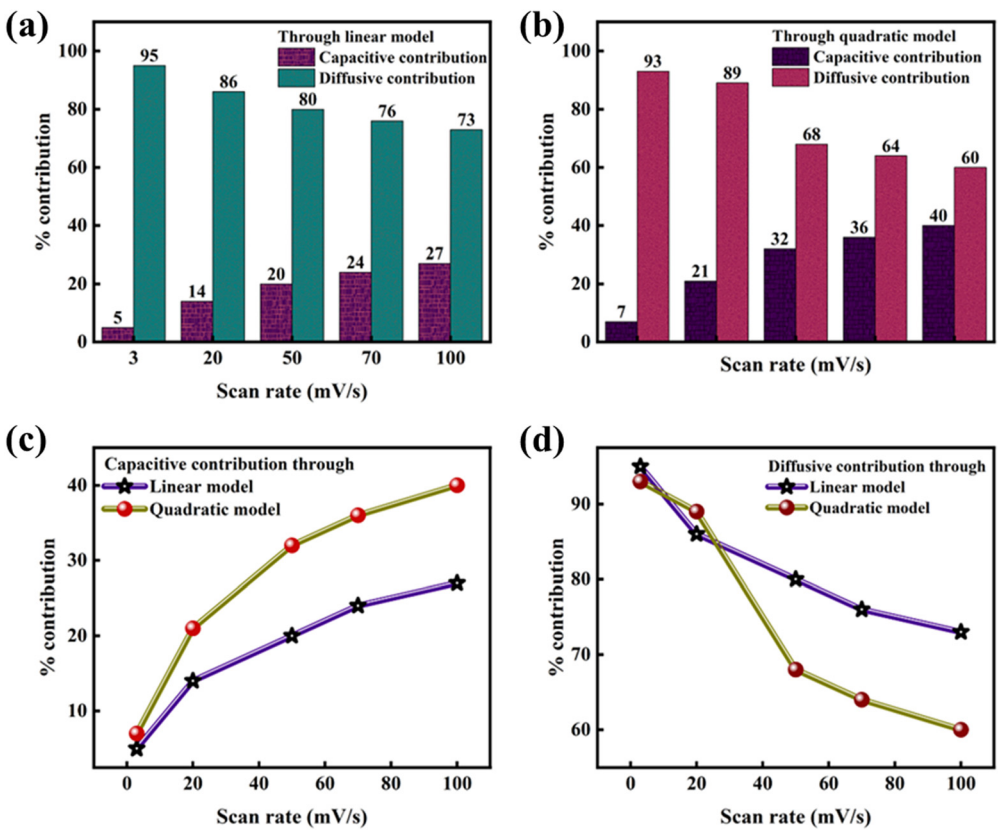

Fig. 9 Bar plots of capacitive and diffusive contributions from (a) linear model and (b) quadratic model. (c) Capacitive contribution *via* linear and quadratic models. (d) Diffusive contribution *via* linear and quadratic models.

diffusive correction to the previous model, which resulted in the quadratic model. The equation is as follows:

$$i(\nu, V) = \beta_1\nu + \beta_2\nu^{1/2} + \beta_2\nu^{3/2} + \varepsilon \quad (7)$$

In the above equation, i, ν and V maintained their original meaning. $\beta_1\nu$ contributes to the capacitive and $\beta_2\nu^{1/2} + \beta_2\nu^{3/2}$ contributes to the diffusive processes. On the experimental data of the device, the quadratic model is further fitted owing to its better performance, as illustrated in Fig. 8(d)–(f). The illustration vividly shows that the model outperforms the linear model on the subject of accurately depicting the amalgamation of contributions from capacitive and diffusive phenomenon, implying an enhanced capacity to eliminate errors. This comprehensive framework improves the understanding of electrochemical mechanisms while offering a more precise overview of currents *via* including novel methodologies that allow identifying discrepancies from theoretical expectations.

Afterwards, the bar plot presented in Fig. 9(a) and (b) highlights the relative contributions from both models, as well as the differential percentage fluctuations at different scan rates. At high scan rates, ions do not get enough time to complete the reaction, increasing the capacitive contribution. Afterwards, we calculated the capacitive and diffusive contributions of both models. Their comparison is presented in Fig. 9(c) and (d). The experimental results for both models show that Pr_2O_3/$C_{18}H_6Cu_3O_{12}$ (50/50) exhibits both capacitor and battery characteristics, with diffusive outcomes outweighing capacitive inputs. At low scan rates, the device is primarily diffusive, suggesting that the battery type's electrode is the one that allows ions to perform faradaic reactions.

7. Conclusion

In this work, Pr_2O_3, $C_{18}H_6Cu_3O_{12}$ and their composites with 3 different ratios were studied and compared for their application as positive electrode materials for HSCs. For the initial evaluation, SEM, XRD and EDX were performed for structural, crystalline and elemental studies. After that, all the samples were explicitly tested in a half cell configuration. Based on the outcomes, Pr_2O_3/$C_{18}H_6Cu_3O_{12}$ (50/50) resulted in a high specific capacity of 2046 C g^{-1} by CV and 1539 C g^{-1} by GCD, demonstrating better rate capability. Because of its distinguished performance, it was coupled with activated carbon in a hybrid device. The maximum energy density was evaluated to be 67 W h kg^{-1} with a corresponding power density of 6114 W kg^{-1}, which is the highest value. The device sustained 98% of its original value after 3000 cycles, indicating considerable cycling stability. The refined performance of this material was attributed to the synergistic effect between Pr_2O_3 and $C_{18}H_6Cu_3O_{12}$, each compensating for the other one's limitation and resulting in enhanced electrochemical activity. These findings assert that the Pr_2O_3/$C_{18}H_6Cu_3O_{12}$ composite is a reliable material for futuristic use in energy storage devices.

Data availability

The data related to this work can be found at the following link: **https://osf.io/ktrb2/files/osfstorage/6720b43150300bb0286297c0**.

Conflicts of interest

There are no conflicts to declare.

Acknowledgements

The authors extend their appreciation to the Researchers Supporting Project Number (RSPD2025R1072), King Saud University, Riyadh, Saudi Arabia.

References

1 M. Chen, Y. Zhang, G. Xing, S.-L. Chou and Y. Tang, *Energy Environ. Sci.*, 2021, **14**, 3323–3351.
2 D.-G. Wang, Z. Liang, S. Gao, C. Qu and R. Zou, *Coord. Chem. Rev.*, 2020, **404**, 213093.
3 A. Rehman, A. Rauf, M. Ahmad, A. A. Chandio and Z. Deyuan, *Environ. Sci. Pollut. Res.*, 2019, **26**, 21760–21773.
4 A. Qazi, F. Hussain, N. A. Rahim, G. Hardaker, D. Alghazzawi, K. Shaban and K. Haruna, *IEEE Access*, 2019, **7**, 63837–63851.
5 M. Minakshi and D. Meyrick, *Electrochim. Acta*, 2013, **101**, 66–70.
6 L. Peng, Y. Zhu, D. Chen, R. S. Ruoff and G. Yu, *Adv. Energy Mater.*, 2016, **6**, 1600025.
7 B. Dunn, H. Kamath and J.-M. Tarascon, *Science*, 2011, **334**, 928–935.
8 D. P. Dubal, O. Ayyad, V. Ruiz and P. Gomez-Romero, *Chem. Soc. Rev.*, 2015, **44**, 1777–1790.
9 B. K. Kim, S. Sy, A. Yu and J. Zhang, *Handbook Clean Energy Systems*, 2015, 1–25.
10 İ. A. Kariper, S. Korkmaz, C. Karaman and O. Karaman, *Fuel*, 2022, **324**, 124497.
11 M. Z. Iqbal, M. M. Faisal and S. R. Ali, *Int. J. Energy Res.*, 2021, **45**, 1449–1479.
12 D. P. Chatterjee and A. K. Nandi, *J. Mater. Chem. A*, 2021, **9**, 15880–15918.
13 A. Muzaffar, M. B. Ahamed, K. Deshmukh and J. Thirumalai, *Renewable Sustainable Energy Rev.*, 2019, **101**, 123–145.
14 A. Ghosh and Y. H. Lee, *ChemSusChem*, 2012, **5**, 480–499.
15 A. Borenstein, O. Hanna, R. Attias, S. Luski, T. Brousse and D. Aurbach, *J. Mater. Chem. A*, 2017, **5**, 12653–12672.
16 M. Z. Iqbal, U. Aziz, M. W. Khan, S. Siddique, M. Alzaid and S. Aftab, *J. Electroanal. Chem.*, 2022, **924**, 116868.
17 Y. Shi, L. Peng, Y. Ding, Y. Zhao and G. Yu, *Chem. Soc. Rev.*, 2015, **44**, 6684–6696.
18 A. Kanwade and P. M. Shirage, *J. Energy Storage*, 2022, **55**, 105692.
19 S. S. Shah, M. A. Aziz and Z. H. Yamani, *Chem. Rec.*, 2022, **22**, e202200018.

20 H. Huang and J.-J. Zhu, *Analyst*, 2019, **144**, 6789–6811.
21 Y. Xin, S. Lu, W. Xu and S. Wang, *New J. Chem.*, 2023, **47**, 211–219.
22 Y. Li, B. Guan, A. Maclennan, Y. Hu, D. Li, J. Zhao, Y. Wang and H. Zhang, *Electrochim. Acta*, 2017, **241**, 395–405.
23 D. B. Bailmare, P. Tripathi, A. D. Deshmukh and B. K. Gupta, *Sci. Rep.*, 2022, **12**, 3084.
24 S. J. Zhu, J. Q. Jia, T. Wang, D. Zhao, J. Yang, F. Dong, Z. G. Shang and Y. X. Zhang, *Chem. Commun.*, 2015, **51**, 14840–14843.
25 A. A. Yadav, A. C. Lokhande, J. H. Kim and C. D. Lokhande, *Int. J. Hydrogen Energy*, 2016, **41**, 18311–18319.
26 R. Rajagopal and K.-S. Ryu, *J. Ind. Eng. Chem.*, 2018, **60**, 441–450.
27 N. Maheswari and G. Muralidharan, *Energy Fuels*, 2015, **29**, 8246–8253.
28 K. T. Kubra, A. Javaid, B. Patil, R. Sharif, A. Salman, S. Shahzadi, S. Siddique and S. Ghani, *Ceram. Int.*, 2019, **45**, 6819–6827.
29 M. N. ur Rehman, T. Munawar, M. S. Nadeem, F. Mukhtar, A. Maqbool, M. Riaz, S. Manzoor, M. N. Ashiq and F. Iqbal, *Ceram. Int.*, 2021, **47**, 18497–18509.
30 X. Wang, C. Yang, T. Wang and P. Liu, *Electrochim. Acta*, 2011, **58**, 193–202.
31 T. Munawar, F. Mukhtar, M. S. Nadeem, S. Manzoor, M. N. Ashiq, M. Riaz, S. Batool, M. Hasan and F. Iqbal, *Ceram. Int.*, 2022, **48**, 19150–19165.
32 S. Chuhadiya, D. Suthar, S. L. Patel and M. S. Dhaka, *Coord. Chem. Rev.*, 2021, **446**, 214115.
33 N. H. N. Azman, M. M. Alias and Y. Sulaiman, *Energies*, 2023, **16**, 7072.
34 B. Matović, J. Pantić, M. Prekajski, N. Stanković, D. Bučevac, T. Minović and M. Čebela, *Ceram. Int.*, 2013, **39**, 3151–3155.
35 H. Jia, Z. Wang, C. Li, X. Si, X. Zheng, Y. Cai, J. Lin, H. Liang, J. Qi, J. Cao, J. Feng and W. Fei, *J. Mater. Chem. A*, 2019, **7**, 6686–6694.
36 Z. Hu, L. Zu, Y. Jiang, H. Lian, Y. Liu, Z. Li, F. Chen, X. Wang and X. Cui, *Polymers*, 2015, **7**, 1939–1953.
37 Q. Wang, Q. Cao, X. Wang, B. Jing, H. Kuang and L. Zhou, *J. Power Sources*, 2013, **225**, 101–107.
38 X. Xiao, T. Li, P. Yang, Y. Gao, H. Jin, W. Ni, W. Zhan, X. Zhang, Y. Cao, J. Zhong, L. Gong, W.-C. Yen, W. Mai, J. Chen, K. Huo, Y.-L. Chueh, Z. L. Wang and J. Zhou, *ACS Nano*, 2012, **6**, 9200–9206.
39 M. Z. Iqbal, M. M. Faisal, S. R. Ali, S. Farid and A. M. Afzal, *Electrochim. Acta*, 2020, **346**, 136039.
40 P. Goel, A. Deep and S. Mishra, *J. Alloys Compd.*, 2023, **934**, 167991.
41 I. Hussain, S. Iqbal, T. Hussain, W. L. Cheung, S. A. Khan, J. Zhou, M. Ahmad, S. A. Khan, C. Lamiel and M. Imran, *Mater. Today Phys.*, 2022, **23**, 100655.
42 S. Kumar, P. H. Weng and Y. P. Fu, *Mater. Today Chem.*, 2022, **26**, 101159.
43 Q. Bi, Q. Ma, K. Tao and L. Han, *Dalton Trans.*, 2021, **50**, 8179–8188.
44 M. Jayachandran, T. Maiyalagan, T. Vijayakumar and B. Gunasekaran, *Mater. Lett.*, 2021, **302**, 130338.
45 G. Li, H. Cai, X. Li, J. Zhang, D. Zhang, Y. Yang and J. Xiong, *ACS Appl. Mater. Interfaces*, 2019, **11**, 37675–37684.
46 S. Xiong, S. Jiang, J. Wang, H. Lin, M. Lin, S. Weng, S. Liu, Y. Jiao, Y. Xu and J. Chen, *Electrochim. Acta*, 2020, **340**, 135956.
47 G. Wang, Z. Yan, N. Wang, M. Xiang and Z. Xu, *ACS Appl. Nano Mater.*, 2021, **4**, 9034–9043.
48 I. Rabani, K. Karuppasamy, D. Vikraman, H.-S. Kim and Y.-S. Seo, *J. Alloys Compd.*, 2021, **875**, 160074.
49 Y. Wang, H. Zhong, L. Hu, N. Yan, H. Hu and Q. Chen, *J. Mater. Chem. A*, 2013, **1**, 2621–2630.
50 U. Shuaib, T. Hussain, R. Ahmad, M. Imranullah, M. Amjad, A. Yasin, I. Shakir and D. J. Kang, *J. Solid State Electrochem.*, 2023, **27**, 715–725.
51 Z. Song, W. Liu, Q. Zhou, L. Zhang, Z. Zhang, H. Liu, J. Du, J. Chen, G. Liu and Z. Zhao, *J. Power Sources*, 2020, **465**, 228266.
52 Y. Wang and Q. Chen, *ACS Appl. Mater. Interfaces*, 2014, **6**, 6196–6201.
53 I. Hussain, S. Iqbal, T. Hussain, Y. Chen, M. Ahmad, M. S. Javed, A. AlFantazi and K. Zhang, *J. Mater. Chem. A*, 2021, **9**, 17790–17800.
54 X. Cao, L. Cui, B. Liu, Y. Liu, D. Jia, W. Yang, J. M. Razal and J. Liu, *J. Mater. Chem. A*, 2019, **7**, 3815–3827.
55 V. Ramasubbu, F. S. Omar, K. Ramesh, S. Ramesh and X. S. Shajan, *J. Energy Storage*, 2020, **32**, 101750.